



1 **Cataclastic deformation of triaxially deformed, cemented mudrock**
2 **(Callovo Oxfordian Clay): an experimental study at the micro/nano scale**
3 **using BIB-SEM**

4 Guillaume Desbois¹, Nadine Höhne¹, Janos L. Urai¹, Pierre Bésuelle², Gioacchino Viggiani³

5 ¹*Structural Geology, Tectonics and Geomechanics, RWTH Aachen University, Lochnerstrasse 4-20,*
6 *52056 Aachen, Germany*

7 ²*CNRS, 3SR, Grenoble, France*

8 ³*Université Grenoble Alpes, 3SR, Grenoble, France*

9 **Abstract**

10 The macroscopic description of deformation and fluid flow in mudrocks can be improved by a better
11 understanding of microphysical deformation mechanisms. Here we use a combination of Scanning
12 Electron Microscopy (SEM) and Broad Ion Beam (BIB) polishing to study the evolution of micro
13 structure in samples of Callovo-Oxfordian Clay that were previously tested in the lab. Digital Image
14 Correlation (DIC) enabled for the measurement of strain fields in the specimens, which were used as a
15 guide to select regions in the sample for BIB-SEM analysis. Microstructures show evidence for
16 dominantly cataclastic mechanisms (intergranular, transgranular, intragranular cracking, grain rotation,
17 clay particle bending) down to nm- scale. At low strain, the dilatant fabric contains individually
18 recognizable open fractures, while at high strain the reworked clay gouge contains broken non-clay
19 grains, with a clear change towards smaller pores than the undeformed material and corresponding
20 resealing of initial fracture porosity.

21 This study might provide a first step towards a micro scale basis for constitutive models of
22 deformation and fluid flow in cemented mudstones

23 **Keywords:** cemented mudrock, Callovo Oxfordian Clay, triaxial deformation, clay microstructure,
24 deformation mechanisms, BIB-SEM, DIC, cataclastic deformation

25 **1 Introduction**

26 Mudrocks constitute up to 80% of the Earth's sedimentary rocks (Stow, 1981). Due to their low
27 permeability and self-sealing properties (Boisson, 2005, Bernier et al., 2007), claystones are



28 considered for nuclear waste disposal and seals for storage in deep geological formations (Salters &
29 Verhoef, 1980; Shapira 1989; Neerdael & Booyazis, 1997; Bonin, 1998; ONDRAF/NIRAS, 2001;
30 NAGRA, 2002; NEA, 2004; ANDRA 2005; IAEA, 2008, Ingram & Urai, 1999). Studies on
31 mechanical and transport properties over long time scales are essential to the evaluation of subsurface
32 integrity. For this, it is generally agreed that a multiscale experimental approach that combines the
33 measurement of the bulk mechanical and transport properties of the specimen with microstructural
34 study to identify deformation mechanisms is required to develop microphysics-based constitutive
35 equations, which can be extrapolated to time scales not available in the laboratory, after comparison
36 with naturally deformed specimens (Morgenstern & Tchalenko 1967; Tchalenko, 1968; Lupini et al.,
37 1981; Rutter et al., 1986; Logan et al., 1979, 1987, 1992; Marone & Scholz, 1989; Evans & Wong,
38 1992; ; Katz & Reches, 2004; Colletini et al., 2009; Haines et al., 2009, 2013; French et al., 2015;
39 Crider, 2015; Ishi, 2016).

40 In the field of rock mechanics and rock engineering, experiments are performed to low strain and short
41 term in order to predict damage and deformation in tunnelling and mining, for example. Here, a
42 macroscopic and phenomenological approach is common, to characterize mechanical and transport
43 properties and to establish the constitutive laws. Microstructures are rarely studied because the
44 strained regions are difficult to find (except macroscopic fractures), and because microstructures
45 below micrometre scales are elusive. However, a microphysics-based understanding of mechanical
46 and fluid flow properties in mudrocks provides a better basis for extrapolating constitutive equations
47 beyond the time scales accessible in the laboratory, so that predictions over the long term can be made
48 less uncertain. This requires integration of measurement of the mechanical and transport properties
49 with microstructures, towards multi-scale description of deformation in mudrocks at low strain.

50 The microstructural geology community studied microstructures in deformed mudrocks to infer
51 deformation mechanisms (Dehandschutter et al., 2004; Gratier et al., 2004; Klinkenberg et al; 2009;
52 Renard, 2012; Robinet et al., 2012; Richard et al., 2015; Kaufhold et al., 2016), but this was limited by
53 the problems with sample preparation. The mechanical properties and related microstructures of
54 natural and experimental high strain fault rocks have been studied extensively (Bos & Spiers, 2001;
55 Faulkner et al., 2003, Marone & Scholz, 1989). For Opalinus Clay (OPA) deformed in laboratory,
56 Nüesch (1991) and Jordan and Nüesch (1989) concluded that cataclastic flow was the main
57 deformation mechanism, with kinking and shearing on R- and P-surfaces at the micro scale, however
58 this was only based on observations with optical microscopy, so the grain scale processes were not
59 resolved. Klinkenberg et al. (2009), demonstrated a correlation between compressive strength and
60 carbonate content of two claystones this correlation is positive for OPA but negative for Callovo
61 Oxfordian Clays (COX). This was explained by the differences in grain size, shape, and spatial
62 distribution of the carbonate (Klinkenberg et al. 2009), cf. Bauer-Plaindoux et al. (1998).



63 Microstructural investigations using BIB-SEM and FIB-TEM in OPA from the main fault in the Mt-
64 Terri Underground Research Laboratory (Laurich et al., 2014) showed that inter- and transgranular
65 microcracking, pressure solution, clay neoformation, crystal plasticity and grain boundary sliding are
66 playing an important role in micro-scale processes during the early stages of faulting in OPA.
67 Cataclastic microstructures are rare and there was an almost complete loss of porosity in micro- shear
68 zones.

69 Digital Image Correlation (DIC) during experimental deformation, in 2D or 3D, measured the
70 displacement fields and quantifies strain over time (Lenoir et al., 2007 Bornert et al., 2010; Bésuelle &
71 Hall, 2011; Dautriat et al., 2011; Wang et al., 2013, 2015; Fauchille et al., 2015; Sone et al., 2015). In
72 samples of rock salt, sand or mudrocks, processes occurring at grain scale can now be studied with
73 high resolution (Hall et al., 2010; Andò et al., 2012; Bourcier et al., 2012, 2013; Wang et al., 2015).
74 On claystones, DIC was used to study swelling in environmental SEM (Wang et al., 2013, 2015;
75 Fauchille et al., 2015) to measure strain at between clay matrix and non clay minerals.

76 Microstructural studies in mudrocks are currently in rapid development driven by the development of
77 ion beam milling tools (e.g. Focussed Gallium Ion Beam (FIB) and Broad Argon Ion Beam (BIB)
78 which allow imaging of mineral fabrics and porosity down to nm- scale in very high quality cross
79 sections with SEM and TEM (Lee et al., 2003; Desbois et al., 2009, 2011, 2013, 2016; Loucks et al.,
80 2009; Curtis et al., 2010; Heath et al., 2011; Klaver et al., 2012; Keller et al., 2011, 2013; Houben et
81 al., 2013, 2014; Hemes et al., 2013, 2015; Laurich et al., 2014; Warr et al., 2014; Song et al., 2016).
82 Serial sectioning allows reconstruction of microstructure in 3D, and cryogenic techniques can image
83 the pore fluid in the samples (Desbois et al., 2013, 2014; Schmatz et al., 2015).

84 Previous work has shown that the mechanical properties of Callovo Oxfordian Clays (COX) do not
85 only depend on the fraction and mineralogy of the clay but also on water content and texture (Bauer-
86 Plaindoux et al., 1998). Chiarelli et al. (2000) showed that COX is more brittle with increasing calcite
87 content and more ductile with increasing clay content and proposed two deformation mechanisms:
88 plasticity induced by slip of clay sheets and induced anisotropic damage as indicated by microcracks
89 at the interface between grains and matrix, however they provided very little microstructural evidence
90 to support this. Gasc-Barbier et al., (2004), Fabre et al., (2006), Chiarelli et al., (2003), Fouché et al.,
91 (2004) report that the COX has an unconfined compressive strength of 20 to 30 MPa and a Young's
92 modulus of 2 to 5 GPa. In the context of underground storage of radioactive wastes, these papers try to
93 predict the mechanical evolution of COX over the period of thousands of years. The effects studied
94 include creep, pore-pressure dissipation, swelling, contraction, chemical effects, pressure solution and
95 force of crystallization. Although these papers develop elaborate constitutive laws, they provide very
96 limited microstructural observations. The need for micromechanical observations was already
97 recognized by Yang et al. (2012) and Wang et al., (2013, 2015) who have conducted deformation



98 experiments under ESEM observation combined with Digital Image Correlation. They have shown
99 how heterogeneous strain fields correlate with microstructure and recognized shear bands and tensile
100 microcracks.

101 For highly overconsolidated claystones from the Variscan foreland thrust belt in the Ardennes and
102 Eifel, Holland et al. (2006) proposed an evolutionary model of the fault zone that developed mainly by
103 mechanical fragmentation of the original claystone's fabric with only minor contribution by diagenetic
104 changes or weathering. In this model, the initial loss of cohesion is driven by kinking, folding and
105 micro-fracturing processes related to an increasing porosity and possibly permeability. Abrasion
106 during progressive deformation increases the amount of clay gouge material, and re-sealing by
107 decrease in pore size and porosity in the clay gouge.

108 In summary, deformation mechanisms in mudrocks are poorly understood. Although as a first
109 approximation the plasticity of cemented and uncemented mudrocks can be described by somewhat
110 similar, pressure dependent constitutive models, the full description of their complex deformation and
111 transport properties would be much improved by better understanding of the microscale deformation
112 mechanisms. There is a wide range of possible mechanisms: intra- and intergranular fracturing,
113 cataclasis, grain boundary sliding, grain rotation and granular flow, crystal plasticity of clays, a the
114 poorly known plasticity of nano-clay aggregates with strong role of clay-bound water, and
115 cementation, fracture sealing and solution- precipitation.

116 This contribution combines stress-strain data, measurement of displacement fields by digital image
117 correlation (DIC) with microstructural investigations in selected areas based on the DIC results. For
118 this, we prepared square millimetre-sized high quality cross sections by broad-ion-beam milling (BIB)
119 followed by scanning electron microscopy (SEM) this allows us to infer microphysical processes of
120 deformation with sub-micron resolution (Figure 1). The two samples used are from the Callovo-
121 Oxfordian Clay (COX, a cemented claystone): one deformed in plane strain compression at 2 MPa
122 confining pressure (COX-2MPa, Bésuelle & Hall, 2011) and another in triaxial compression at 10
123 MPa confining pressure (COX-10MPa, Lenoir et al., 2007). Specimens were taken from the Bure site
124 in Meuse-Haute Marne in France, and belong to the clay-rich facies of COX.

125 **2 Material studied and DIC-derived strain fields**

126 Mechanical experiments were performed on two COX samples collected at the ANDRA Underground
127 Research Laboratory located at Bure (Meuse/ Haute Marne, Eastern France) at approximately 550 m
128 below the ground surface (Boisson, 2005). The clay fraction (illite/smectite, illite, chlorite) is 40–45%,
129 carbonate (mostly calcite) and quartz 25–35% and 30%, respectively and minor feldspar, mica and
130 pyrite.



131 The details of these experiments including instrumentation set-ups, boundary conditions and DIC
132 interpretations are comprehensively described in Bésuelle and Hall (2011) and Lenoir et al. (2007).
133 This contribution presents mostly the microstructural analysis performed on these previously
134 deformed two samples.

135 The first sample considered in this study (COX-2MPa) was tested in plane strain compression at 2
136 MPa confining pressure. 2D DIC was performed on consecutive photographs of one side of the
137 specimen (in the plane of deformation) throughout the test. Further details are given in Bésuelle and
138 Hall (2011). The second sample (COX-10MPa) was tested in triaxial compression at 10 MPa
139 confining pressure. 3D DIC was performed on consecutive x-ray images of the specimen obtained in a
140 synchrotron throughout the test. Further details are given in Lenoir et al. (2007) – please note that in
141 this publication this sample is referred to as ESTSYN01.

142 In the following, the relevant findings in Bésuelle & Hall (2011) and Lenoir et al. (2007) are
143 summarized:

144 (1) The prismatic sample COX-2MPa was tested in plane strain compression in a true triaxial
145 apparatus at a constant value of $\sigma_3 = 2$ MPa. The size of the specimen is 50 mm in the vertical
146 direction, which is the direction of major principal stress (1), 30 mm in the direction of
147 intermediate principal stress (2), and 25 mm in the direction of minor principal stress (3). The
148 test was displacement-controlled, with a constant rate of displacement (in the direction 1) of
149 $1.25 \mu\text{m/s}$, i.e., a strain rate of $2.5 \cdot 10^{-5} \text{ s}^{-1}$ (see Bésuelle & Hall 2011 for further details). Figure
150 2a shows the evolution of the differential stress ($\sigma_1 - \sigma_3$) vs. axial strain (specimen shortening
151 divided by its initial height). The curve shows a first stress peak at 0.02 axial strain, followed
152 by a strong stress drop. Then, a slow stress increase is observed, followed by a second stress
153 drop at 0.42 axial strain. After, the stress is quite constant. As shown in Figures 2b and 2c,
154 these two stress drops are associated with major failure by faulting in the specimen. The crack
155 that appeared during the second drop is conjugate to the first crack set, which appeared at the
156 first drop. This set of conjugate fractures, at an angle of 20° to 45° about the direction 1, will
157 be referred to as “main synthetic fractures” in the following sections. The DIC-derived strain
158 fields in Figures 2b and 2c also show that the development of each single conjugate fracture is
159 accompanied by relay zones with a set of antithetic fractures. Moreover, the fracture appearing
160 during the second stress drop (Fig. 2c) is also reactivating the first fracture and its associated
161 antithetic fractures. At this resolution (pixel size is $10 \mu\text{m}$), the set of conjugate fractures and
162 the associated antithetic fractures are the major features of localized deformation: they
163 represent zones where the sample was sheared with damaged zones having a thickness of



164 about 60 μm . Dilatancy was also measured in the damaged zones mentioned above (see
165 volumetric strain fields, Figs. 2b and 2c).

166

167 (2) The cylindrical sample COX-10MPa (10 mm in diameter and 20 mm in height) was sheared in
168 triaxial compression at a confining pressure of 10 MPa. The test was carried out under
169 tomographic monitoring at the European Synchrotron Radiation Facility (ESRF) in Grenoble,
170 (France), using an original experimental set-up developed at Laboratoire 3SR at the University
171 of Grenoble Alpes (France).. Complete 3D images of the specimens were recorded throughout
172 the test using x-ray microtomography (voxel size was 14 μm). The test was displacement-
173 controlled, with a displacement rate of 0.05 $\mu\text{m/s}$, i.e., an axial strain rate of $2.5 \cdot 10^{-6} \text{ s}^{-1}$. The
174 stress-strain curve (Figure 3.a) shows only one stress peak at an axial strain of 0.04. The peak
175 stress is followed by a major stress drop corresponding to the formation of a shear fracture
176 (referred to as “main synthetic fracture” in the following sections) oriented at an angle of 30-
177 40° about the direction of the principal stress σ_1 (the DIC-based maximum shear strain fields
178 are given in Fig. 3b). The DIC-derived volumetric strain fields (not shown here, see Lenoir
179 2006) indicate that the shear fracture is accompanied by some slight dilatancy.

180 3 Methods: BIB-SEM imaging of deformed microstructures

181 Sub-samples were selected to represent areas with different strain history based on the DIC analysis.
182 For COX-2MPa, three BIB cross sections were prepared around the conjugate fractures in areas with
183 different amount of diffuse strain (at the resolution of DIC), antithetic fractures (ROI-2, ROI-3 and
184 ROI-4; Figures 4.b, 6.b, c, d and 7) and a fourth one in a region without measurable strain (ROI-1;
185 Figures 4.b and 6.a). For COX-10MPa, two BIB-SEM analyses were done around the single shear
186 fracture (Figures 4.e and 6.e, f).

187 Sub-samples were first stabilized with epoxy, extracted with a low speed diamond saw in dry
188 conditions, pre-polished dry using SiC polishing papers and BIB polished by using a JEOL SM-09010
189 cross-section polisher (for 8 h, $1 \cdot 10^{-3} - 1 \cdot 10^{-4} \text{ Pa}$, 6 kV, 150 μA). BIB cross-sections are all prepared
190 parallel both to the principle stress (σ_1) direction and perpendicular to the shear displacement plane.
191 BIB cross sections of about 1.5 mm^2 (Figures 6 and 7) were imaged with a Supra 55-Zeiss SEM (SE2
192 and BSE detectors at 20 kV and $\text{WD} = 8 \text{ mm}$). Further details of the method are given in (Klaver et
193 al., 2012, 2015, Houben et al., 2013, 2014, Hemes et al., 2013, 2015, Desbois et al., 2016)



194 **4 Results**

195 **4.1 Overview of microstructures**

196 The sub-sample without measurable strain (i.e. ROI-1_COX-2MPa, Figure 6a) shows non-clay
197 minerals in a clay matrix with a weak shape preferred orientation parallel to bedding (perpendicular to
198 the experimental σ_1). The clay matrix contains submicron pores typical of compaction and diagenesis,
199 with a power law distribution of pore sizes. Pores commonly have very high aspect ratio, with the long
200 axis oriented sub-parallel to the bedding. These characteristics are very similar to those in the
201 undeformed COX sample (Figure 5, cf. Robinet et al. 2012).

202 In all other BIB cross-sections (Figures 6.c-f and 7), both samples show damaged microstructures. At
203 the sample scale, three different types of fracture are identified: (i) the main synthetic fracture (section
204 2), (ii) antithetic fractures (Figure 6) and (iii) joints sub-parallel to the main fracture. The material
205 between the fractures zones has very similar microstructure to the undeformed COX.

206 **4.2 Detailed description of microstructures**

207 **4.2.1 Arrays of antithetic fractures**

208 In COX-2MPa the antithetic fractures (Figure 7) are of two different types. *Type I* is located only in
209 the clay matrix (Figure 8.a), with apertures up to few micrometres, with boundaries closely matching -
210 suggesting that these are opening mode fractures (Mode I). *Type II* fractures consist of a damage zone
211 with thickness up to 25 μm (Figure 8.e, f, g, h, i) containing angular fragments of non-clay minerals
212 and clay aggregates, (Figure 8.h), sometimes with preferred orientation parallel to the fracture. The
213 transition between the damage zone and the undeformed host rock is sharp (Figure 8.f, g, h, i). In
214 relay zones the fracturing becomes so intense that the clay matrix is fragmented into clay-size
215 fragments (Figure 8.i). Porosity in these relay zones is locally much higher and pores much larger than
216 in undeformed COX. Fracture boundaries usually do not match (Figure 8.h). Figure 8.e shows
217 examples where parts of broken non-clay minerals can be matched.

218 COX-10MPa, we observed the two types of antithetic fractures mentioned above. Antithetic fractures
219 of *Type I* are very similar (indicated in Figure 6.f) to those in COX-2MPa but rare, whereas antithetic
220 fractures of *Type II* contain a wider damage zone in comparison to those in COX-2MPa, in which the
221 average grain size and the pore size is significantly smaller, consistent with stronger cataclasis at high
222 confining pressure. In parts of the damage zones interpreted to be restraining sections, pores in the
223 reworked clay aggregates cannot be resolved in the SEM.



224 In both samples, the fragments between the arrays of antithetic fractures show only minor deformation
225 indicated by fractured grains of organic matter (Figure 8.b), calcite (Figure 8.d, c) or quartz (Figure
226 8.d). Visible relative rotation of parts of fractured grain is rare (Figure 8.d).

227 **4.2.2 Synthetic fractures**

228 The synthetic fractures are the regions that localized most of strain and have the thickest damage zone
229 (Figures 2 and 3). Here, COX-2MPa and COX-10MPa show very similar microstructures. The grain
230 (fragment) size of non-clay minerals is significantly smaller than in the host rock and their sizes are
231 poorly sorted. Non-clay minerals have also angular or/and chipped edges (Figures 9, 10 and 12).
232 Locally, grains in the damaged zone show trans-granular fractures (Figure 10.c and 12.a). In parts of
233 the damage zone, dilatancy and a strong increase in connected porosity (ROI-4_COX-2MPa, Figure 9
234 and ROI-2_COX-10MPa, Figure 10) is indicated by epoxy impregnation. In other parts, (ROI-
235 1_COX-10MPa) strongly reworked clay matrix is not impregnated and shows no pores visible at the
236 resolution of image (83.8 nm pixel size in Figure 11.b, c).

237 For COX-2MPa, the DIC analysis shows that the conjugated synthetic fractures form a complex
238 network of fracture's branches at region where they both intersect (Figure 2.c). The ROI-3_COX-
239 2MPa sub-sample (Figure 4.c) covers two of these branches. Microstructural analysis of these two
240 branches in ROI-3_COX-2MPa show similar microstructures, with only the fracture apertures being
241 different (Figure 6.c).

242 In both COX-2MPa and COX-10MPa, the damage zone of the synthetic fractures contains an open
243 fracture (Figures 9, 10 and 12), with apertures of 50 - 70 μm . These large open fractures are filled with
244 epoxy, have matching boundaries and never crosscut the non-clay minerals in the damage zone.
245 Similar fractures are found in COX-2MPa but parallel to the antithetic fractures, with jagged
246 morphologies, matching walls never crossing the non-clay minerals (Figure 8.b, c, e). These fractures
247 are not resolved by DIC.

248 **5 Discussion**

249 **5.1 Artefacts caused by drying and unloading**

250 Claystones are sensitive to changes in hydric conditions that can lead to the shrinkage or the swelling
251 of the clay matrix (Galle, 2001; Kang et al., 2003; Soe et al., 2007; Gasc-Barbier & Tessier, 2007;
252 Cosenza et al., 2007; Pineda et al., 2010; Hedan et al., 2012; Renard, 2012; Desbois et al., 2014).



253 The DIC analysis is not affected by this because the images were acquired during deformation of
254 preserved (wet) samples. SEM analysis is done on samples which have been deformed and unloaded,
255 followed by slow drying and further dehydration in the high vacuum of the BIB and SEM. In COX-
256 10MPa, this is illustrated by Figures 4.d and 4.e. Figure 4.d shows the sample at the end of the
257 deformation experiment, whereas Figure 4.e shows the same sample but about 10 years later, both
258 imaged with X-ray. The comparison of Figures 4.e and 4.e shows that cracks developed parallel to the
259 bedding and that the apertures of fractures developed during the deformation became larger. These are
260 interpreted to result from unloading and shrinkage during drying and aging of specimens. We infer
261 that similar changes occurred in COX-2MPa: the wider damage zones in conjugate synthetic fractures
262 imaged by SEM (Figure 6.c, d) compared the width estimated from the DIC analysis corroborates this
263 interpretation.

264 The fractures in the fragments between the arrays of antithetic fractures (Figure 8.b,c,d) are not
265 present in the low strain ROI-1_COX-2MPa, and they are sub parallel to σ_1 , strongly suggesting they
266 are formed by experimental deformation.

267 In contrast, antithetic fractures of *Type II* (Figures 6, 7 and 8.e-i) are interpreted to develop during
268 deformation because: (i) the internal microstructures and fabrics are damaged and (ii) DIC recorded a
269 clear localization of strain in these. Though the antithetic fractures of *Type I* are not clearly recognized
270 at the resolution of DIC, most of these in COX-2MPa (Figure 8.a) are interpreted to develop during
271 deformation because they are oblique to the bedding and parallel to the antithetic fractures of *Type II*
272 (Figure 6, 7 and 8.f-g). One exception is the antithetic fractures of *Type I* observed in ROI-1_COX-
273 10MPa (Figure 6.e), which is parallel to bedding. Mode I fractures sub-parallel to the main synthetic
274 fractures are less easy to interpret: they may be related to the rotation of blocks between the antithetic
275 fractures (Kim et al., 2004). Cryogenic techniques to preserve wet fabrics combined with ion beam
276 milling and cryo-SEM (Desbois et al., 2008, 2009, 2013, 2014) is the dedicated technique to solve this
277 question in the future.

278 **5.2 Deformation mechanisms**

279 The first, and perhaps surprising conclusion based on the observations above is the dominantly
280 cataclastic deformation in Callovo-Oxfordian Clay at confining pressures up to 10 MPa.
281 Microfracturing, producing fragments at a range of scales and reworking into a clay-rich cataclastic
282 gouge during frictional flow are the main processes in both samples. This is accompanied by dilatancy
283 by microfracturing of the original fabric, but also by progressive decrease of porosity and pore size in
284 the gouge with the non-clay particles embedded in reworked clay.



285 Although in many cases the initial fractures propagate around the hard non-clay grains, there is also
286 significant fracturing of the hard non-clay minerals (e.g. Figure 8.b-d). This can be due to local stress
287 concentrations at contacts between adjacent non-clay clay minerals, or because the clay matrix is so
288 strongly cemented that it can transmit stresses sufficient to fracture calcite and quartz grains. Broken
289 non-clay minerals can displace or rotate with respect to each other (Figure 8.d) with local dilatancy
290 during deformation (Figure 2.b), in agreement with the interpretation of DIC measurements in
291 Bésuelle & Hall (2011) and Lenoir et al. (2007).

292 In COX-2MPa, the propagation of antithetic fractures of Type I (Figure 8.a) is predominantly in the
293 clay matrix (Figure 8.a). This is in agreement with the smaller strain in comparison to antithetic
294 fractures of Type II. Antithetic fractures of Type II contain angular non-clay grains with size smaller
295 than those in the host rock. We interpret these as evidence for comminution by grain fracturing.
296 Matching broken grains (Figure 8.e) are rare and in agreement with high strain cataclastic flow.
297 Fragments of clay aggregates in the antithetic fractures of Type II are much less coherent (Figure 8.h)
298 and more porous than the undeformed COX (Figure 8.i), indicating strong remolding by cataclastic
299 flow, and perhaps also plastic deformation of phyllosilicates. Here, pore morphologies are not
300 compatible with drying - induced deformation only, and we infer that these developed during
301 deformation.

302 Microstructures in the main synthetic fractures, both in COX-2MPa (Figure 9) and COX-10 MPa
303 (Figures 10 and 12), are similar. Angular non-clay minerals in the reworked clay matrix have a wide
304 range of grain sizes, smaller than those in the host rock. These characteristics are typical for cataclasis
305 (Passchier & Trouw, 2005). COX-2MPa the cataclastic gouge seems to be more porous than in COX-
306 10 MPa; this is as expected for the lower mean stress, but firm conclusion require further study to
307 exclude that this is an unloading and drying effect. For COX-10MPa, the porosity in clay matrix is
308 clearly reduced in comparison to the one in the host rock: most pores, if present, are below the
309 resolution of SEM (Figure 10 and 11). The mechanism of this compaction during shearing is
310 interpreted to be a combination of cataclasis of the cemented clay matrix, and shear-induced
311 rearranged the clay particles around the fragments of non-clay particles.

312 **6 Conclusions**

313 The integration of bulk stress-strain data, the analysis of displacement fields by 3D digital image
314 correlation (DIC) with Broad Ion Beam cutting and Scanning Electron Microscopy (BIB-SEM) is a
315 powerful multiscale method to study the deformation behaviour of mudstones.



316 We studied samples of Callovo-Oxfordian Clay (COX) subjected to triaxial compression at 2 MPa
317 and 10MPa confining pressure. DIC was used to locate regions deformed to different states of strain
318 and BIB-SEM allows microstructural investigations of mineral and porosity fabrics down to
319 nanometre scale.

320 Microstructures show evidence for dominantly cataclastic mechanisms (intergranular, transgranular,
321 intragranular cracking, grain rotation, clay particle bending) down to nm- scale.

322 At low strain, the dilatant fabric contains individually recognizable open fractures, while at high strain
323 in shear fractures the reworked clay gouge evolves towards smaller pores than the undeformed
324 material and corresponding resealing of initial fracture porosity. This shear induced resealing is more
325 important at the higher confining pressure.

326 This study provides a first step towards a microphysical basis for constitutive models of deformation
327 and fluid flow in cemented mudstones, with an improved extrapolation of these models for long time
328 scales.

329 In the future, the microstructures on experimentally deformed specimens needs to be compared with
330 the microstructures in naturally deformed claystones (Laurich et al.; 2014) in order to extrapolate the
331 constitutive models to long time scales.

332 **Acknowledgements**

333 We thank ANDRA for providing samples.

334 **References**

335 Andò E., Hall S.A., Viggiani G., Desrues J., Besuelle P. (2012). Grain-scale experimental investigation of
336 localised deformation in sand: a discrete particle tracking approach. *Acta Geotechnica*, 7: 1–13.

337 ANDRA (2005a). Evaluation of the feasibility of a geological repository in an argillaceous formation.
338 Meuse/Haute Marne site. Dossier 2005, Argiles - Report Series, ANDRA.

339 Bauer-Plaindoux C., Tessier D., Ghoreychi M. (1998). Propriétés mécaniques des roches argileuses carbonatées:
340 importance de la relation calcite-argile. *C. R. Acad. Sci. Paris, Sciences de la Terre et des planètes / Earth and
341 Planetary Sciences*, 326, 231-237.

342 Bernier et al. (2007). Fractures and Self-healing within the Excavation Disturbed Zone in Clays (SELFRAC).
343 Final report, European Commission, CORDIS Web Site, EUR 22585, 2007, 56p.

344 Bésuelle P. & Hall S.A. (2011). Characterization of the Strain Localization in a Porous Rock in Plane Strain
345 Condition Using a New True-Triaxial Apparatus. *Advances in bifurcation and degradation in geomaterials*,
346 Springer Series in geomechanics and geoengineering, Volume 11:345-352.

347 Boisson, J. Y. (2005): Clay Club Catalogue of Characteristics of Argillaceous Rocks,
348 OECD/NEA/RWMC/IGSC (Working Group on measurement and Physical understanding of Groundwater flow



- 349 through argillaceous media) august 2005 Report NEA no. 4436 (Brochure and CD-Rom including data base).
 350 OECD/NEA Paris, France, 72.
- 351 Bonin B. (1998). Deep geological disposal in argillaceous formations: studies at the tournemire test site. *Journal*
 352 *of Contaminant Hydrogeology*, 35: 315-330.
- 353 Bornert M., Vales F., Gharbi H., Nguyen Minh D. (2010). Multiscale full-field strain measurements for
 354 micromechanical investigations of the hydromechanical behaviour of clayey rocks, *Strain*, 46(1): 33-46.
- 355 Bos B., Spiers C.J. (2001). Experimental investigation into the microstructural and mechanical evolution of
 356 phyllosilicate-bearing fault rock under conditions favouring pressure solution. *Journal of Structural Geology*, 23:
 357 1187-1202.
- 358 Bourcier M., Bornert M, Dimanov A., heripré E., Raphanel J.L. (2013). Multiscale experimental investigation of
 359 crystal plasticity and grain boundary sliding in synthetic halite using digital image correlation. *Journal of*
 360 *Geophysical Research, Solid Earth*, 118(2): 511.526.
- 361 Bourcier M., Dimanov A., Héripéré E., Raphanel J.L., Bornert M., Desbois G. (2012). Full field investigation of
 362 salt deformation at room temperature: cooperation of crystal plasticity and grain sliding. In *mechanical behavior*
 363 *of salt VII*, Berest, Ghoreychi, Hadj-Hassen & Tijani (eds), Taylor & Francis group, London: 37 – 43.
- 364 Chiarelli A.S., J.F. Shao, N. Hoteit (2003) Modeling of elastoplastic damage behavior of a claystone.
 365 *International Journal of Plasticity* 19:23-45
- 366 Chiarelli A.S., Ledesert B., Sibal M., Karami M., Hoteit N. (2000). Influence of mineralogy and moisture
 367 content on plasticity and induced anisotropic damage of a claystone: application to nuclear waste disposal. *Bull.*
 368 *Soc. géol. France*, 171(6), 621- 627.
- 369 Collettini C., Niemeijer A., Viti, C. Marone C. (2009). Fault zone fabric and fault weakness. *Nature*, 462, 907-
 370 10.
- 371 Cosenza P., Ghorbani A., Florsch N., Revil A. (2007). Effects of Drying on the Low-Frequency Electrical
 372 Properties of Tournemire Argillites. *Pure and applied Geophysics*, 164(10): 2043-2066.
- 373 Crider J.G. (2015). The initiation of brittle faults in crystalline rock. *Journal of Structural Geology*, 77: 159-174.
- 374 Curtis M.E., Ambrose R.J., Sondergeld C.H., Rai C.S. (2010). Structural Characterization of Gas Shales on the
 375 Micro- and Nano-Scales, Canadian Unconventional Resources and International Petroleum Conference. Society
 376 of Petroleum Engineers, Calgary, Alberta, Canada, p. 15.
- 377 Dautriat J., Bornert M., Gland N., Dimanov A., Raphanel J. (2011). Localized deformation induced by
 378 heterogeneities in porous carbonate analysed by multi-scale digital image correlation. *Tectonophysics*, 503 (1-2):
 379 100-116.
- 380 Dehandschutter, B., Vandycke, S., Sintubin, M., Vandenberghe, N., Gaviglio, P., Sizun, J.-P. & Wouters, L.
 381 (2004). Microfabric of fractured Boom Clay at depth: a case study of brittle-ductile transitional clay behaviour.
 382 *Applied Clay Science*, 26(1-4): 389-401.
- 383 Desbois G., J.L. Urai, F. Pérez-Willard, Z. Radi, S. van Offern, I. Burkart, P.A. Kukla, U. Wollenberg (2013).
 384 Argon broad ion beam tomography in cryogenic scanning electron microscope: a novel tool for the investigation
 385 of preserved representative microstructures. Application to rock salt and other sedimentary rocks.. *Journal of*
 386 *Microscopy*, 249(3): 215-235.
- 387 Desbois G., Urai J.L., Hemes S., Schröppel B., Schwarz J.-O., Mac M., Weiel D. (2016). Multiscale analysis of
 388 porosity in diagenetically altered reservoir sandstone from the Permian Rotliegend (Germany). *Journal of*
 389 *Petroleum Science and Engineering*, 140: 128-148.
- 390 Desbois G., Urai J.L. and Kukla P.A. (2009). Morphology of the pore space in claystones - evidence from
 391 BIB/FIB ion beam sectioning and cryo-SEM observations. *E-Earth*, 4 :15-22..



- 392 Desbois G., Urai J.L., Burkhardt C., Drury M.R., Hayles M., Humbel B. (2008). Cryogenic vitrification and 3D
 393 serial sectioning using high resolution cryo-FIB SEM technology for brine-filled grain boundaries in halite: first
 394 results. *Geofluids*, 8: 60-72.
- 395 Desbois G., Urai J.L., Hemes S., Brassinnes S., De Craen M., Sillen X. (2014). Nanometer-scale pore fluid
 396 distribution and drying damage in preserved clay cores from Belgian clay formations inferred by BIB-cryo-
 397 SEM. *Engineering Geology*, 170:117-131.
- 398 Desbois G., Urai J.L., Kukla P.A., Konstanty J. and Baerle C. (2011). High-resolution 3D fabric and porosity
 399 model in a tight gas sandstone reservoir: a new approach to investigate microstructures from mm- to nm-scale
 400 combining argon beam cross-sectioning and SEM imaging. *Journal of Petroleum Science and Engineering*, 78:
 401 243-257.
- 402 Evans B. & Wong T.-F. (1992). *Fault mechanics and transport properties of rocks*. Academic Press, International
 403 Geophysics, volume 51, pp524
- 404 Fabre, Géraldine, Frédéric Pellet (2006) Creep and time-dependent damage in argillaceous rocks *International*
 405 *Journal of Rock Mechanics & Mining Sciences* 43:950–960
- 406 Fauchille A.-L., Hedan S., Prêt D., Cosenza P., Valle V., Cabrera J. (2015). Relationships between desiccation
 407 cracking behavior and microstructure of the Tournemire clay-rock by coupling DIC and SEM methods. In
 408 *Geomechanics from micro to macro*. Soga et al. (Eds): 1421-1424.
- 409 Faulkner D.R., Lewis A.C., Rutter E.H. (2003). On the internal structure and mechanics of large strike-slip fault
 410 zones: field observations of the Carboneras fault in southeastern Spain. *Tectonophysics*, 367: 235–251
- 411 Fouché Olivier, Hervé Wright, Jean-Michel Le Cléac'h, Pierre Pellenard (2004) Fabric control on strain and
 412 rupture of heterogeneous shale samples by using a non-conventional mechanical test *Applied Clay Science*
 413 26:367–387
- 414 French M.E., Chester F.M., Schester J.S. (2015). Micromechanisms of creep in clay-rich gouge from the Central
 415 Deforming Zone of the San Andreas Fault, *Journal of Geophysical Research, Res. Solid Earth*, 120: 827–849.
- 416 Galle C. (2001). Effect of drying on cement-based materials pore structure as identified by mercury intrusion
 417 porosimetry: A comparative study between oven-, vacuum-, and freeze-drying. *Cement and concrete research*,
 418 31(19): 1467-1477.
- 419 Gasc-Barbier M. and Tessier D. (2007). Structural Modifications of a Hard Deep Clayey Rock due to Hygro-
 420 Mechanical Solicitations. *Int. J. Geomech.*, 7(3), 227–235.
- 421 Gasc-Barbier M., S. Chanchole P. Bérest (2004) Creep behavior of Bure clayey rock. *Applied Clay Science* 26
 422 449–458
- 423 Gratier J.P., Jenatton L., Tisserand D., Guiguet R. (2004). Indenter studies of the swelling, creep and pressure
 424 solution of Bure argillite. *Applied Clay Sciences*, 26: 459-472.
- 425 Haines S.H., Kaproth B., Marone C., Saffer D., Van der Pluijm B. (2013). Shear zones in clay-rich fault gouge:
 426 A laboratory study of fabric development and evolution. *Journal of structural geology*, 51: 206-225.
- 427 Haines S.H., Van der Pluijm B., Ikari M.J., Saffer D.M., Marone C. (2009). Clay fabric intensity in natural and
 428 artificial fault gouges: Implications for brittle fault zone processes and sedimentary basin clay fabric evolution.
 429 *Journal of Geophysical research*, 114, B05406
- 430 Hall S., Bornert M., Desrues J., Pannier Y., Lenoir N., Viggiani G. and Bésuelle P. (2010). Discrete and
 431 Continuum analysis of localised deformation in sand using X-ray CT and Volumetric Digital Image Correlation,
 432 *Géotechnique*, 60: 315–322.



- 433 Heath J.E., Dewers T.A., McPherson B.J.O.L., Petrusak R., Chidsey T.C., Rinehart A.J., Mozley P.S. (2011).
434 Pore networks in continental and marine mudstones: Characteristics and controls on sealing behavior. *Geosphere*
435 7: 429-454.
- 436 Hedan S., Cozensa P., Valle V., Dudoignon P., Fauchille A.-L., Cabrera J. (2012). Investigation of the damage
437 induced by desiccation and heating of Tournemire argillite using digital image correlation. *International Journal*
438 *of rock mechanics and mining sciences*, 51: 64-75.
- 439 Hemes S., Desbois G., Urai J.L., De Craen M. and Honty M. (2013). Variations in the morphology of porosity in
440 the Boom Clay Formation: insights from 2D high resolution, BIB-SEM imaging and Mercury injection
441 Porosimetry. *The Netherlands Journal of Geosciences*, 92(4): 275-300.
- 442 Hemes S., Desbois G., Urai J.L., Schröppel B., Schwarz J-O (2015). Multi-scale characterization of porosity in
443 Boom Clay (HADES, Mol, Belgium) using a combination of μ -CT, BIB-SEM and serial FIB-SEM techniques.
444 *Microporous and Mesoporous Materials* 208, 1-20
- 445 Holland M., Urai J.L., van der Zee W., Stanjek H., Konstanty J. (2006). Fault gouge evolution in highly
446 overconsolidated claystones. *Journal of Structural Geology*, 28: 323–332.
- 447 Houben M.A., Desbois G. and Urai J.L. (2013). Pore morphology and distribution in the shaly facies of Opalinus
448 clay (Mont Terri, Switzerland) : insights from representative 2D BIB-SEM investigations on mm- to nm- scales.
449 *Applied Clay Sciences*, 71(C): 82-97.
- 450 Houben M.A., Desbois G. and Urai J.L. (2014). A comparative study of representative 2D microstructures in
451 Shaly and Sandy facies of Opalinus Clay (Mont Terri, Switzerland) inferred from BIB-SEM and MIP methods.
452 *Marine and Petroleum Geology*, 49: 143-161.
- 453 IAEA (2008). The safety case and safety assessment for radioactive waste disposal. Draft safety guide.
454 International atomic energy agency, report No DS 355, Vienna.
- 455 Ingram, G.M. and J.L. Urai (1999). Top-seal leakage through faults and fractures; the role of mudrock
456 properties. *Geological Society Special Publications*, 158: 125-135.
- 457 Ishii, E. (2016), Far-field stress dependency of the failure mode of damage-zone fractures in fault zones: Results
458 from laboratory tests and field observations of siliceous mudstone, *Journal of Geophysical Research, Solid*
459 *Earth*, 121, doi:10.1002/2015JB012238.
- 460 Jordan P. and Nüesch R. (1989) Deformation behavior of shale interlayers in evaporite detachment horizons,
461 Jura overthrust, Switzerland. *Journal of Structural Geology*, 11(7): 859-871.
- 462 Kang M-S., Watabe Y. and Tsuchida T. (2003). Effect of Drying Process on the Evaluation of Microstructure of
463 Clays using Scanning Electron Microscope (SEM) and Mercury Intrusion Porosimetry (MIP). *Proceedings of*
464 *The Thirteenth (2003) International Offshore and Polar Engineering Conference Honolulu, Hawaii, USA, May*
465 *25–30, 2003*
- 466 Katz O. and Reches Z. (2004). Microfracturing, damage, and failure of brittle granites. *Journal of Geophysical*
467 *Research*, 109, B01206.
- 468 Kaufhold A., Halisch M., Zacher G., Kaufhold S. (2016). X-ray computed tomography investigation of
469 structures in Opalinus Clay from large-scale to small-scale after mechanical testing. *Solid Earth*, 7: 1171-1183.
- 470 Keller L., Schuetz P., Erni R., Rossell, M.D., Lucas, F., Gasser, Ph., Holzer L. (2013). Characterization of multi-
471 scale microstructural features in Opalinus Clay. *Microporous and Mesoporous Materials*, 170 : 83-94.
- 472 Keller L.M., Holzer L., Wepf R., Gasser P. (2011). 3D geometry and topology of pore pathways in Opalinus
473 clay: Implications for mass transport. *Applied Clay Science* 52: 85-95.
- 474 Kim Y-S, Peacock D.C.P, Sanderson D.J. (2004). Fault damage zones. *Journal of Structural Geology*, 26: 503-
475 517.



- 476 Klaver J., Desbois G., Littke R., Urai J.L. (2015). BIB-SEM characterization of pore space morphology and
 477 distribution in postmature to overmature samples from the Haynesville and Bossier Shales, Marine and
 478 Petroleum Geology, 59: 451-466.
- 479 Klaver J., Desbois G., Urai J.L. and Littke R. (2012). BIB-SEM study of porosity of immature Posidonia shale
 480 from the Hils area, Germany. International Journal of Coal Geology, 103: 12-25.
- 481 Klinkenberg M., Kaufhold S., Dohrmann R., Siegesmund S. (2009). Influence of carbonate microfibrils on the
 482 failure strength of claystones. Engineering Geology 107: 42-54.
- 483 Laurich B., Urai J.L., Desbois G., Vollmer C., Nussbaum C. (2014). Microstructural evolution of an incipient
 484 fault zone in Opalinus Clay: Insights from an optical and electron microscopic study of ion-beam polished
 485 samples from the Main Fault in the Mont Terri underground research laboratory. Journal of Structural Geology,
 486 67: 107–128.
- 487 Lee M.R., Bland P.A., Graham G. (2003). Preparation of TEM samples by focused ion beam (FIB) techniques:
 488 applications to the study of clays and phyllosilicates in meteorites. Mineralogical Magazine, 67(3): 581-592.
- 489 Lenoir N., Bornert M., Desrues J., Besuelle P., Viggiani G. (2007). Volumetric digital image correlation applied
 490 to X-ray microtomography images from triaxial compression tests on argillaceous rock. Strain, 43: 193-205.
- 491 Logan J.M., Dengo C.A., Higgs N.G., Wang Z.Z. (1992). Fabrics of Experimental Fault Zones: Their
 492 Development and Relationship to Mechanical Behavior, in: Evans, B., Wong, T. (Eds.), Fault Mechanics and
 493 Transport Properties of Rocks- A Festschrift in Honor of W. F. Brace. Academic Press, pp. 33–67.
- 494 Logan J.M., Friedman M., Higgs N., Dengo C., Shimamoto T. (1979). Experimental studies of simulated gouge
 495 and their application to studies of natural fault zones, in: Proceedings of Conference VIII on Analysis of Actual
 496 Fault Zones in Bedrock. US Geological Survey, Open File Report, pp. 79–1239.
- 497 Logan J.M., Rauenzahn K.A. (1987). Frictional dependence of gouge mixtures of quartz and montmorillonite on
 498 velocity, composition and fabric. Tectonophysics, 144: 87–108.
- 499 Loucks R.G., Reed R.M., Ruppel S.C., Jarvie D.M. (2009). Morphology, Genesis, and Distribution of
 500 Nanometer-Scale Pores in Siliceous Mudstones of the Mississippian Barnett Shale. Journal of Sedimentary
 501 Research 79: 848-861.
- 502 Lupini J.F., Skinner A.E., Vaughan P.R. (1981). The drained residual strength of cohesive soils. Géotechnique
 503 31(2):181-213.
- 504 Marone C. and Scholz C.H. (1989). Particle-size distribution and microstructures within simulated fault gouge.
 505 Journal of Structural Geology, 11(7): 799-814.
- 506 Morgenstern N.R., Tchalenko J.S. (1967). Microscopic structures in kaolin subjected to direct shear.
 507 Geotechnique, 17: 309-328.
- 508 Nagra (2002). Technischer Bericht 02-03, Projekt Opalinuston, Synthese der geowissenschaftlichen
 509 Untersuchungsergebnisse.
- 510 NEA (2004). Post-closure safety case for geological repositories. Nature and purpose. OECD/NEA, No 3679,
 511 Paris. France.
- 512 Neerdael B., Boyazis J.P. (1997). The Belgium underground research facility: status on the demonstration issues
 513 for radioactive waste disposal in clay. Nuclear engineering and design, 176: 89-96.
- 514 Nüesch R., (1991): Das mechanische Verhalten von Opalinuston. PhD Thesis, ETH Zürich. 244 p.
- 515 ONDRAF/NIRAS (2001). SAFIR 2. Safety Assessment and Feasibility Interim Report 2. NIROND 2001-06.
- 516 Passchier C.W., Trouw R.A.J. (2005). Microtectonics. Springer, 366 pp



- 517 Pineda J., Romero E., Gómez S., Alonso E. (2010). Degradation effects at microstructural scale and their
 518 consequences on macroscopic behaviour of a slightly weathered siltstone. In *Geomechanics and Geotechnics.*
 519 *From Micro to Macro, Two Volume Set*, Edited by Malcolm Bolton, CRC Press 2010, Pages 73–78.
- 520 Renard F. (2012). Microfracturation in rocks: from microtomography images to processes. *Eur. Phys. J. Appl.*
 521 *Phys.*, 60: 24203
- 522 Richard J., Gratier J.P., Doan M.-L., Boullier A.-M., Renard F. (2015). Rock and mineral transformations in a
 523 fault zone leading to permanent creep: Interactions between brittle and viscous mechanisms in the San Andreas
 524 Fault. *Journal of Geophysical Research, Solid Earth*, 119: 8132–8153,
- 525 Robinet J.C., Sardini P., Coelho D., Parneix J.-C., Dimitri P., Sammartino S., Boller E., Altmann S. (2012).
 526 Effects of mineral distribution at mesoscopic scale on solute diffusion in a clay-rich rock: Example of the
 527 Callovo-Oxfordian mudstone (Bure, France). *water resources research*, 48, W05554.
- 528 Rutter E. H. , Maddock R. H. , Hall S. H. , White S. H. (1986). Comparative microstructures of natural and
 529 experimentally produced clay-bearing fault gouges. *Pure and Applied Geophysics* January 1986, Volume
 530 124, Issue 1, pp 3-30
- 531 Salters V.J.M. & Verhoef P.N.W. (Eds.) 1980. *Geology and nuclear waste disposal*, Vol. No.1 of *Geologica*
 532 *Ultraiectina* Special Publication, Instituut voor Aardwetenschappen der Rijksuniversiteit te Utrecht, Institute of
 533 Earth Sciences, Utrecht, 399pp.
- 534 Schmatz J., berg S., urai J., Ott H. (2015). Nano-scale imaging of pore-scale fluid-fluid-solid contacts in
 535 sandstone, *Geophysical Research Letters*, 42: 2189 – 2195
- 536 Shapira J.P. (1989). Long-term waste management: present status and alternatives. *Nuclear instruments and*
 537 *methods in Physics Research*, A280: 568-582
- 538 Soe A.K.K., Osada M., Takahashi M., Sasaki T. (2009). Characterization of drying-induced deformation
 539 behaviour of Opalinus Clay and tuff in no-stress regime. *Environmental Geology*, 58(6): 1215-1225.
- 540 Sone H., Morales L.F., Dresen G. (2015). Microscopic observations of shale deformation from in-situ
 541 deformation experiments conducted under a scanning electron microscope. *ARMA*: 15-27.
- 542 Song Y., Davy C.A., Bertier P., Troadec D. (2016). Understanding fluid transport through claystones from their
 543 3D nanoscopic pore network. *Microporous and Mesoporous Materials*, 228: 64-85.
- 544 Stow D.A.V. (1981). Fine-grained sediments: Terminology. *Quarterly Journal of engineering Geology London*,
 545 14: 243-244.
- 546 Tchalenko J.S., Morgenstern N.R. (1967). Microscopic Structures in Kaolin Subjected to Direct Shear.
 547 *Géotechnique* 17: 309–328.
- 548 Wang L. L., Bornert M., Chancole S., Heripré E., Yang S. (2015). Micromechanical experimental investigation
 549 of mudstones. *Géotechnique letters* 4, 306-309.
- 550 Wang L. L., Bornert M., Chancole S., Yang S., Heripré E., Tanguy A., Caldemaïson D. (2013). Micro-scale
 551 experimental investigation of the swelling anisotropy of the Callovo- Oxfordian argillaceous rock. *Clay*
 552 *Minerals*, 48: 391–402.
- 553 Warr L.N., Wojatschke J., Carpenter B.M., Marone C., Schleicher A.M., van der Pluijm B. a. (2014). A “slice-
 554 and-view” (FIB–SEM) study of clay gouge from the SAFOD creeping section of the San Andreas Fault at 2.7
 555 km depth. *Journal of Structural Geology*, 69: 234–244.
- 556 Yang, D. S., Bornert, M., Chanchole, S. et al. (2012). Dependence of elastic properties of argillaceous rocks on
 557 moisture content investigated with optical full-field strain measurement techniques. *Int. J. Rock Mech. Mining*
 558 *Sci.* 53, 45–55.



559 **Figure captions**

560 **Figure 1:** Drawing of the experimental concept used for the investigation of experimentally deformed fine-
561 grained mudrocks from bulk-scale to nm-scale. The example is based on a triaxial deformation test (10 MPa
562 confining pressure) performed on a cylindrical Callovo-Oxfordian Clay, where displacement fields were
563 followed by volumetric DIC on X-ray microtomography images (after Lenoir et al., 2007;).

564 **Figure 2:** Results of deformation test done on sample COX-2MPa. (a): deviator stress vs. axial strain response.
565 The red star indicates the state of sample when BIB-SEM microstructural analyses are done. (b) and (c):
566 incremental volumetric strain fields (VSF) and maximum shear strain fields (SSF) fields for deformation
567 increment 1-2 and 3-4 indicated in (a) after DIC. After Bésuelle et al. (2011).

568 **Figure 3:** Results of deformation test done on sample COX-10MPa. (a): deviator stress vs. axial strain response.
569 The red star indicates the state of sample when BIB-SEM microstructural analyses are done. (b) and (c):
570 incremental maximum shear strain fields for deformation increment 1-2 and 2-3 indicated in (a) interpreted after
571 DIC. After Lenoir et al. (2007).

572 **Figure 4:** Selection of differently strained areas (ROI) highlighted from DIC analysis on samples COX-2MPa
573 (a-b) and COX-10MPa (c-e), for BIB-SEM microstructural analyses. (b): for COX-2MPa, four ROI were
574 analysed: three at conjugate synthetic fractures in areas with different amount of diffuse strain and antithetic
575 fractures (ROI-2, ROI-3 and ROI-4) and one in a region without measurable strain. (e): for COX-10MPa, two
576 ROI were analysed both around the single synthetic shear fracture. (d) shows the X-ray radiography of the
577 sample taken directly at the end of the deformation test. (e) shows the X-ray radiography of the same sample but
578 taken about 10 years after the end of the deformation: drying cracks developed following the bedding and the
579 aperture of the single shear fracture became larger. Orientation of σ_1 and of the bedding are indicated in red.

580 **Figure 5:** (a): BSE SEM micrograph of the typical mineral fabric in undeformed COX. (b): SE2 SEM
581 micrograph of a detail from (a) showing the typical pore fabric in undeformed COX.

582 **Figure 6:** BSE SEM micrographs of the BIB cross-sections' overviews of COX-2MPa (a-d) and COX-10MPa
583 (e-f) at differently strained areas (ROI) highlighted from DIC analysis in Figure 4. High strained ROI (c-f),
584 display damaged microstructures, where three different types of fracture are identified: (1) the main synthetic
585 fracture, (2) antithetic fractures oriented about 60° to the main fracture and (3) joints sub-parallel to the main
586 synthetic fracture. These fracture are respectively indicated by 1, 2, 3 numbers in the figure. Orientation of the
587 principle stress (σ_1) is indicated in red. Dashed yellow lines indicate the boundaries of the BIB polished areas.

588 **Figure 7:** Larger field of BSE SEM micrograph of the BIB cross-section's overview at ROI-1 in COX-2MPa
589 sample. It shows the network of antithetic fractures (indicated by number 1) oblique to the principle main
590 synthetic fracture (indicated by number 2). Orientation of the principle stress (σ_1) is indicated in red. Dashed
591 yellow lines indicate the boundaries of the BIB polished areas.



592 **Figure 8:** Detailed microstructures in sample COX-2MPa. (a): a fracture running parallel to the antithetic
593 fractures and at the interfaces between non-clay mineral and clay matrix. (b) and (c): intragranular fractures (i)
594 and transgranular fractures (ii) at impingement of non-clay minerals. (d): a broken quartz grain showing
595 evidence for rotation of its broken fragments. (e): incipient of flow of broken non-clay mineral within the
596 antithetic fractures. (f) and (g): parts of antithetic fractures displaying thick damaged fabrics made of broken
597 grains and clay matrix fragments. (h): Detail from (g). (i): Detail from (f) showing the denser and deformed
598 fabric of a part of the clay matrix squeezed between a quartz grain located in the damaged fabric and the
599 boundary with the host rock. In (f-i), the damaged zone is related to a higher porosity in comparison to the host
600 rock. Orientation of σ_1 is indicated in red. Dashed yellow lines indicate the boundaries between the damaged
601 fabric and the host rock, and also some grain boundaries. Qtz: quartz; Cc.: calcite; OM: organic matter. Black
602 squares in (f) are missing pictures.

603 **Figure 9:** Detailed microstructure close the main fracture (indicated by number 1) in sample COX-2MPa. The
604 main fracture displays internal damaged fabric made of fragments of broken non-clay minerals and clay matrix.
605 Close to the main synthetic fracture, the host rock displays jagged joints sub-parallel to the main synthetic
606 fracture (indicated by number 3) starting and ending at antithetic fracture (indicated by number 2). Orientation of
607 the principle stress (σ_1) is indicated in red. The dashed yellow line indicates the boundary between the damaged
608 fabric and the host rock.

609 **Figure 10:** Microstructures of ROI-1 in sample COX-10MPa. (a-c): The damaged fabric within the main
610 fracture (1) is made of fragments of non-clay minerals derived from the dense, tight clay matrix. (a): the large
611 open fracture in the middle of the main fracture (black) is interpreted to develop after the experiment by
612 unloading or/and drying (see Section 5.1 for details). (c): some grains within the damaged fabric, but close to the
613 boundary between the damaged fabric and the host rock, show transgranular fracturing (ii). Orientation of the
614 principle stress (σ_1) is indicated in red. The dashed yellow lines indicate the boundaries between the damaged
615 fabric and the host rock.

616 **Figure 11:** Detail of Figure 10.b. Microstructures (ROI-1_COX-10MPa) showing detail of porosity in BSE
617 SEM micrograph (a) and SE2 SEM micrograph (b). At the resolution of the SEM micrograph, the damaged
618 fabric appears very low porous in comparison to the host rock. The dashed yellow line indicates the boundary
619 between the damaged fabric (left) and the host rock (right).

620 **Figure 12:** Detailed microstructures at ROI-2 in sample COX-10MPa. (a-c): The damaged fabric within the
621 main synthetic fracture (indicated by number 1) is made of fragments of non-clay minerals and clay matrix
622 derived from the host rock. (a): some grains within the damaged fabric, but close to the boundary between the
623 damaged fabric and the host rock, show transgranular fracturing (ii). Detailed observations in (b) and (c) (SE2
624 SEM and BSE SEM micrographs of the same sub-area, respectively) show that parts of the damaged fabric
625 display (1) porous island, where pores are between the fragments of non-clay and clay matrix; whereas other
626 parts display (2) low porous islands made of fragment of non-clay minerals embedded in a dense, tight clay
627 matrix. Pores within the porous island can be either filled with epoxy (in deep black pixel values) or not.



628 Orientation of σ_1 is indicated in red. The dashed yellow lines indicate the boundaries between the damaged
 629 fabric and the host rock.

630 **Figures**

631

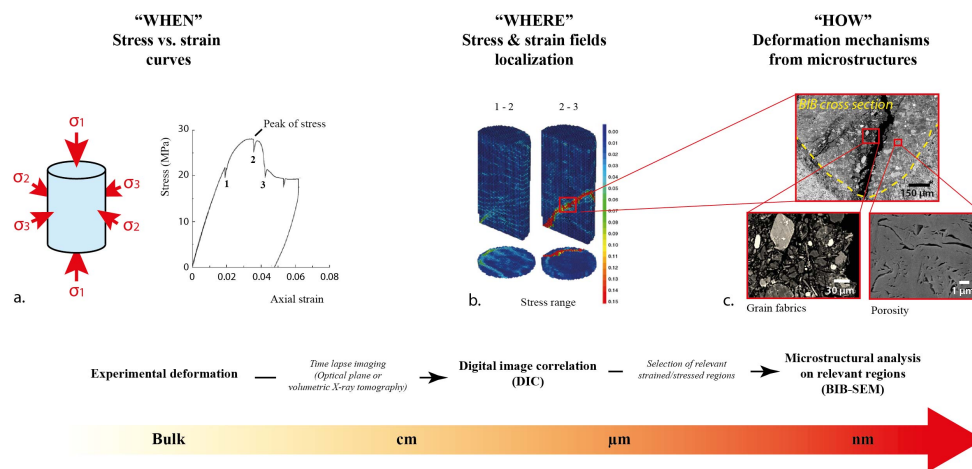
632

633

634

635

636



637

638

Figure 1

639

640

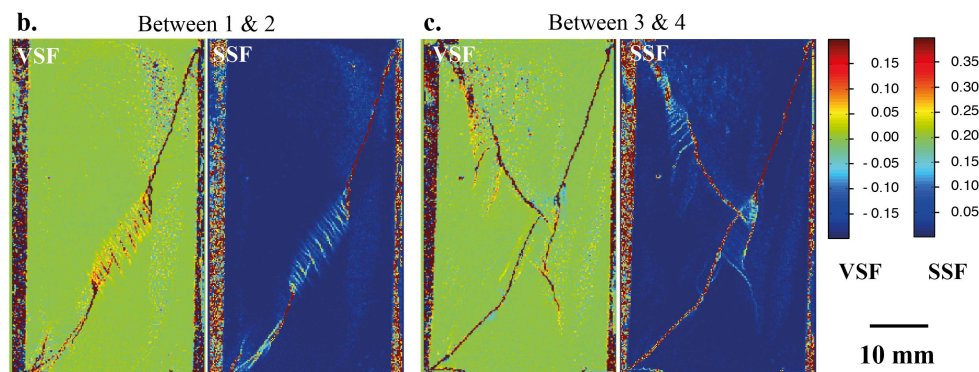
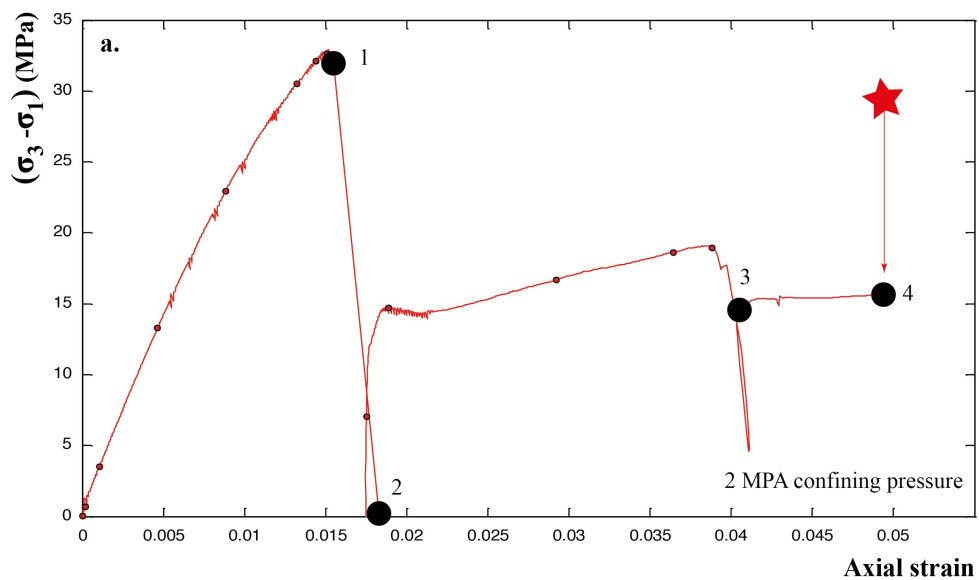
641

642

643



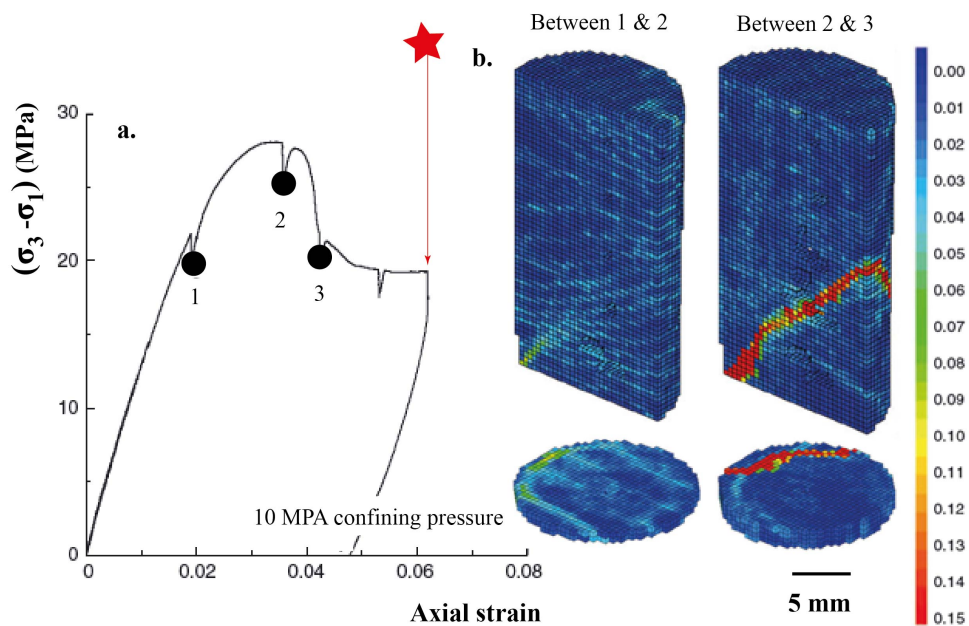
644
 645
 646



647 VSF: Volumetric strain field ; SSF: Maximum shear stress field
 648 **Figure 2**



649
650
651
652
653
654



655
656
657
658
659
660
661

Figure 3

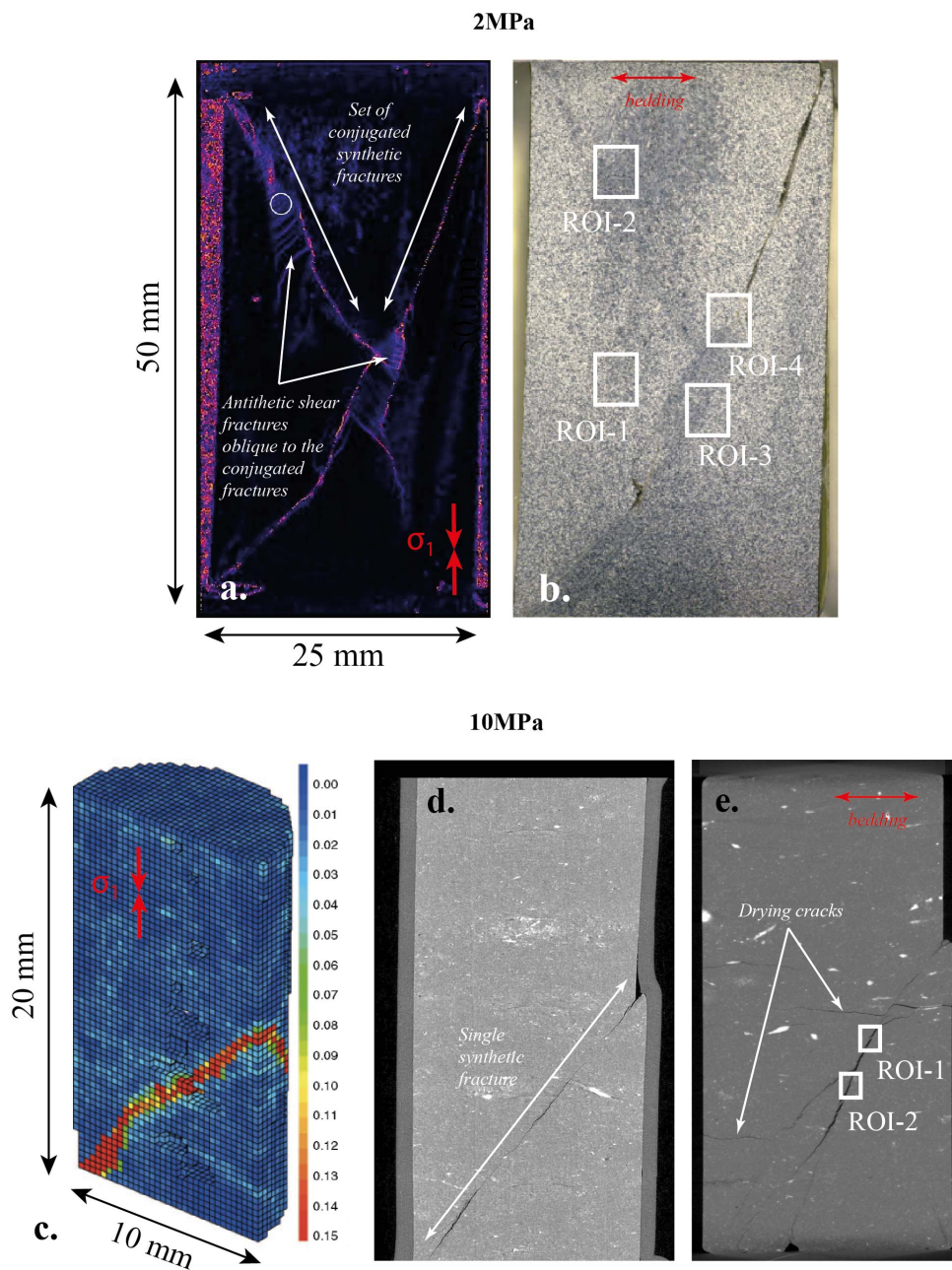
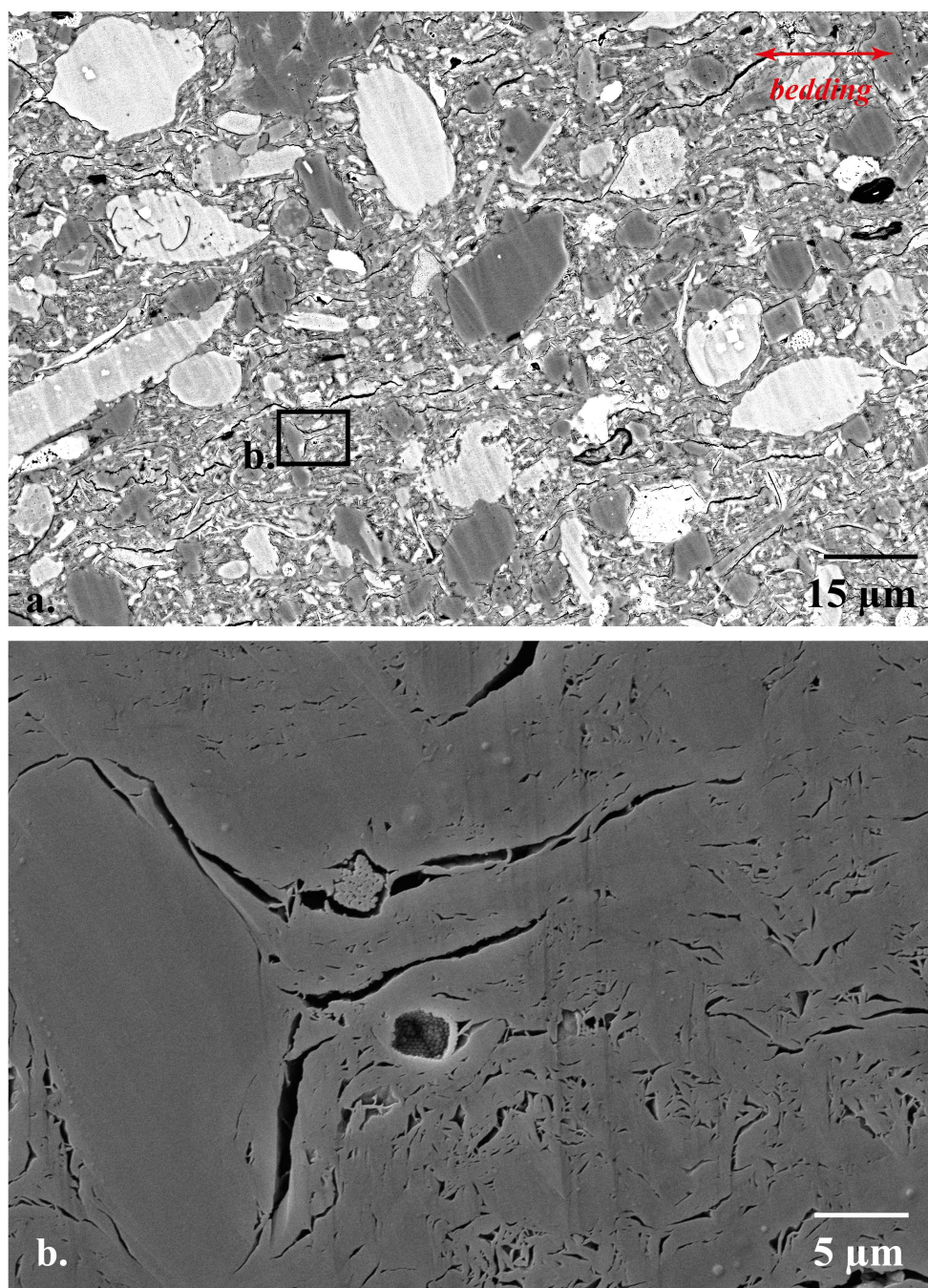


Figure 4



665

666

667

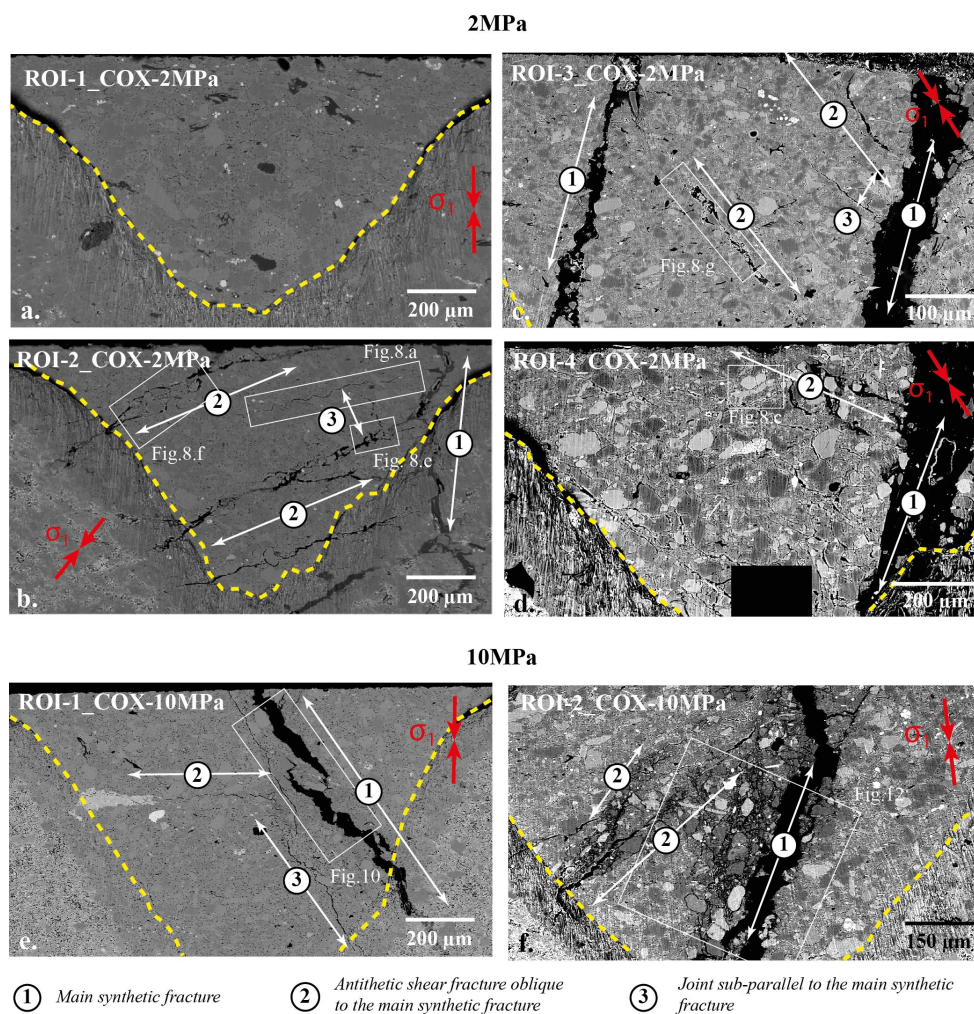
Figure 5



668

669

670



671

672

Figure 6

673

674

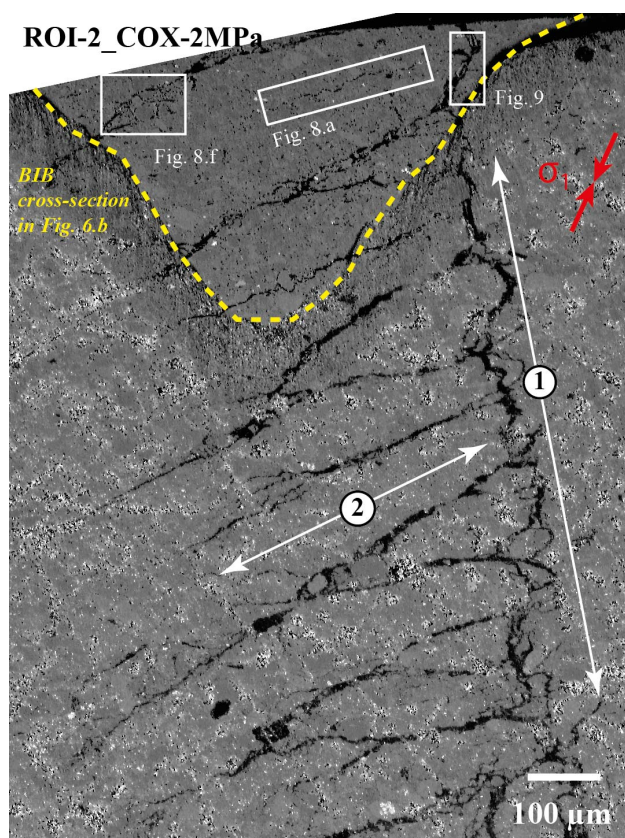


675

676

677

678

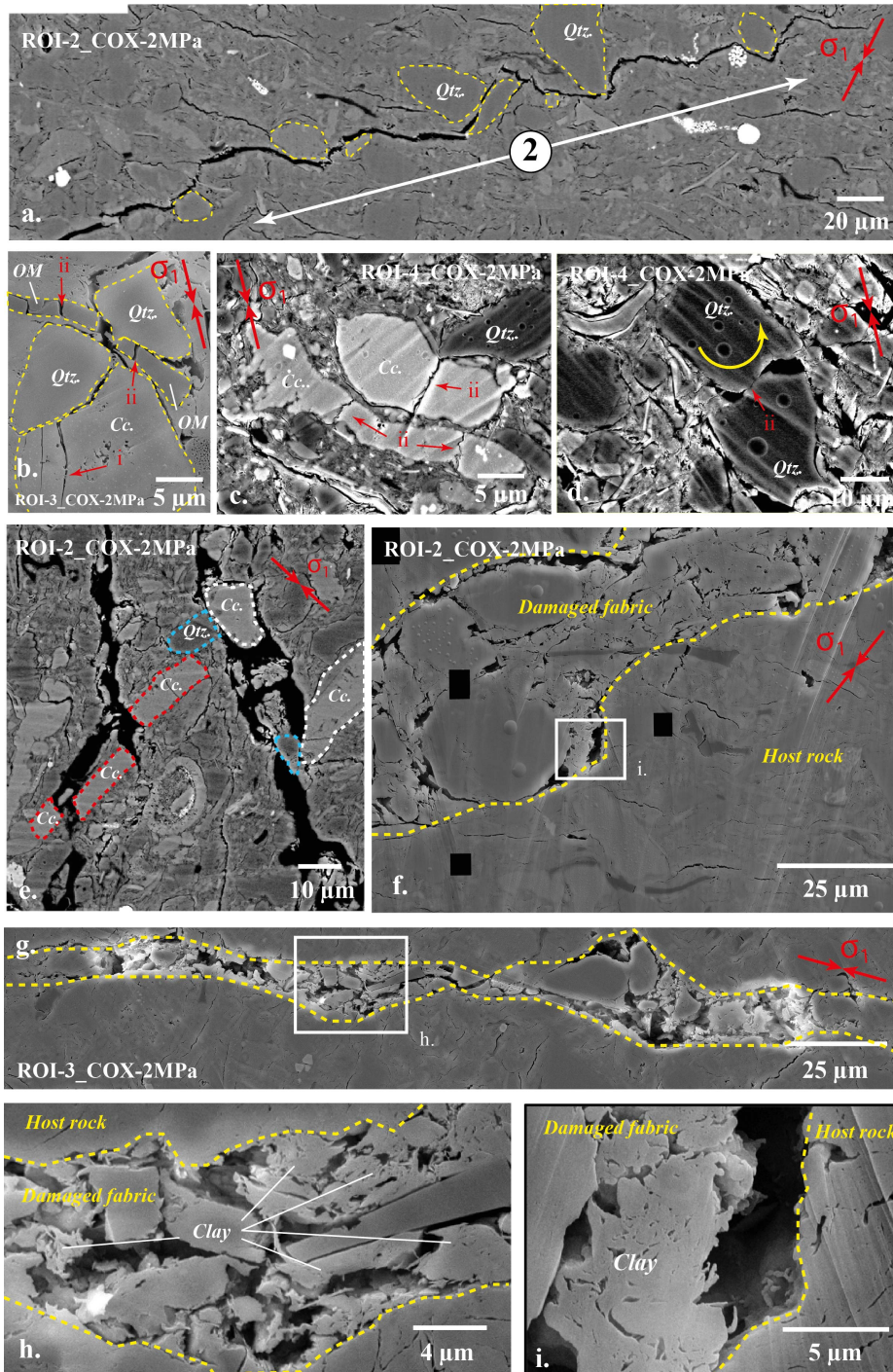


679

680

681

Figure 7



682

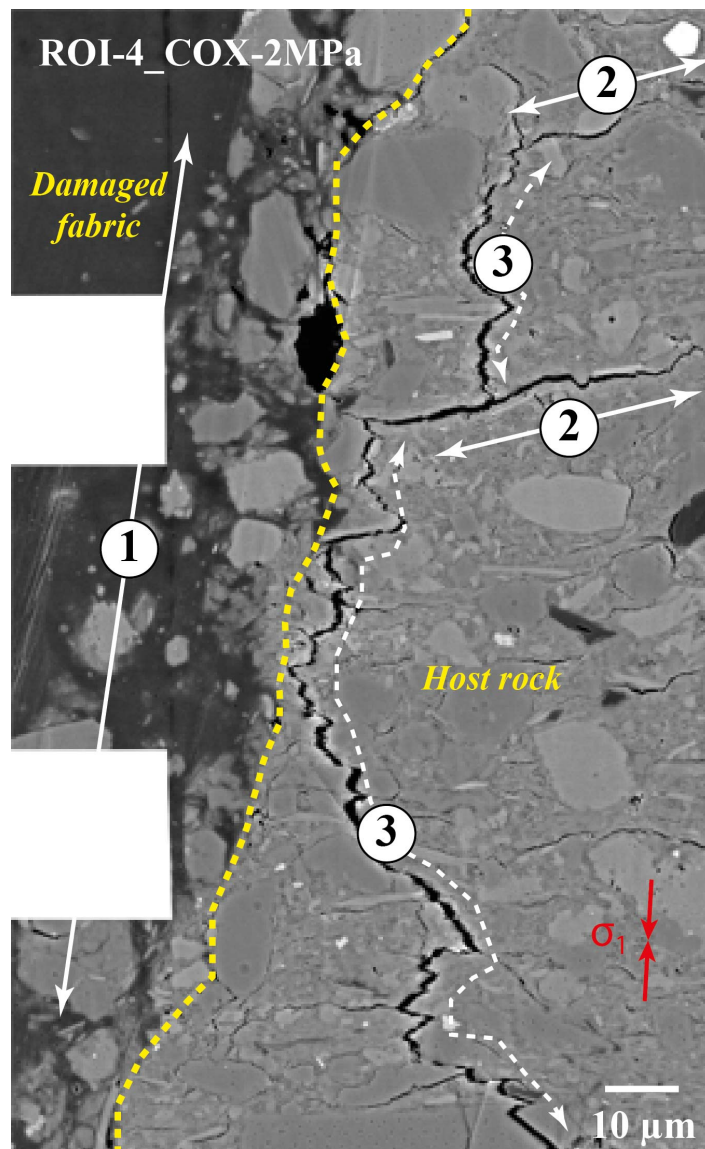
683

Figure 8



684

685



686

687

688

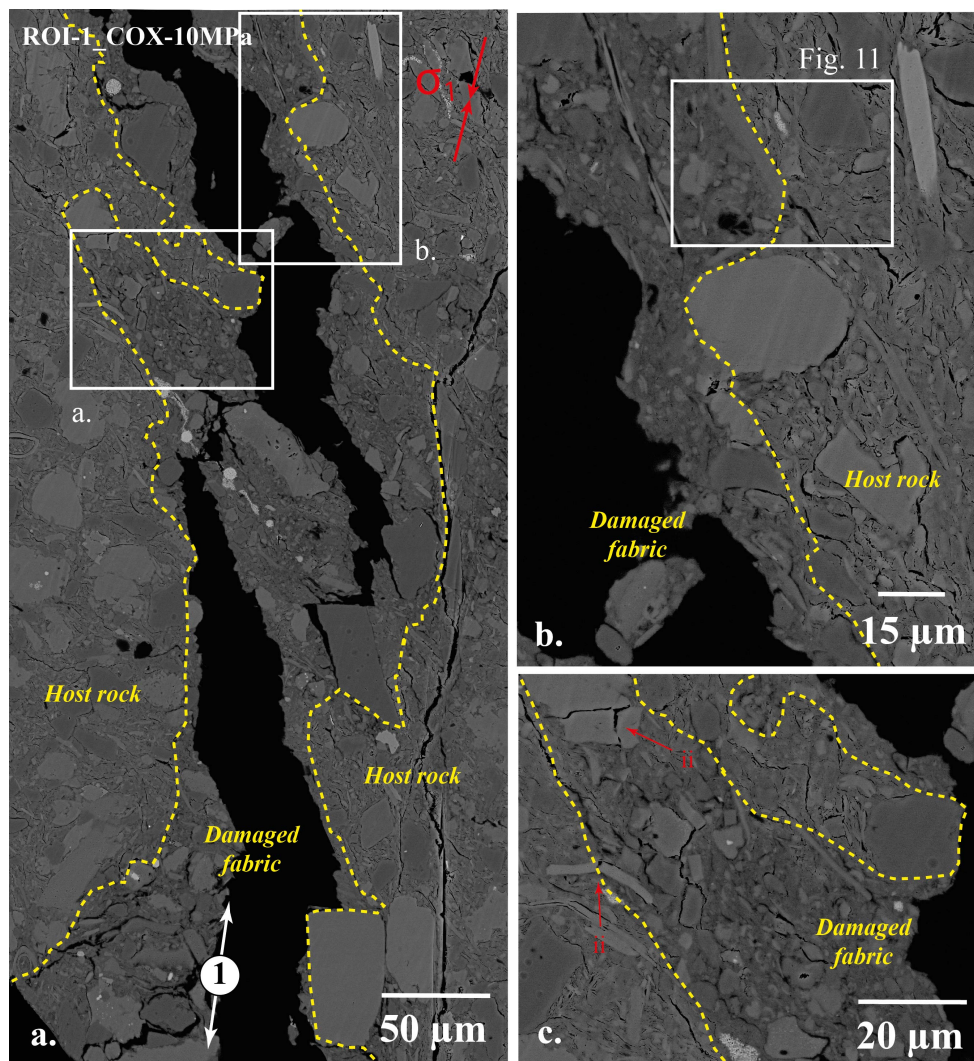
689

Figure 9



690

691

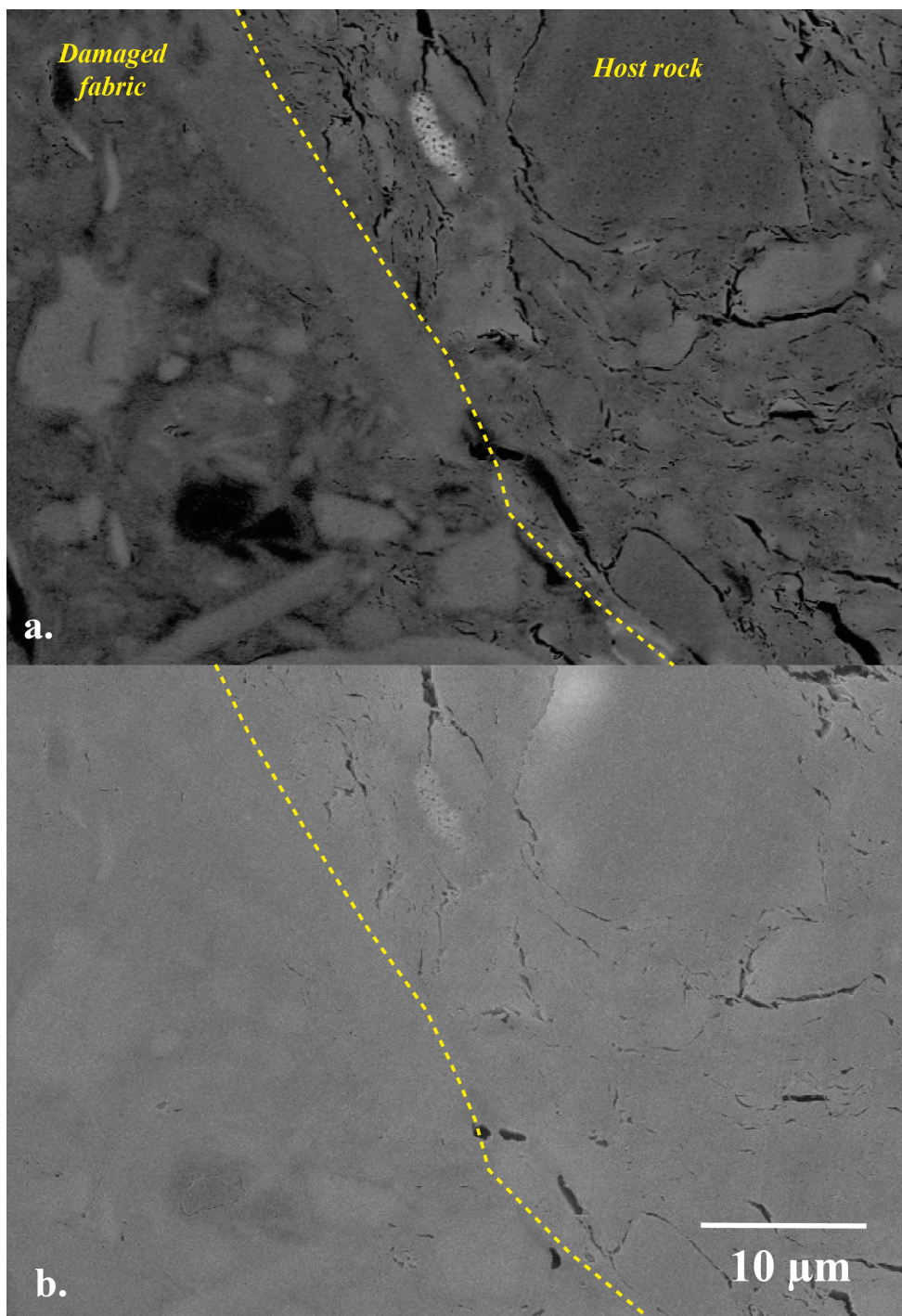


692

693

694

Figure 10



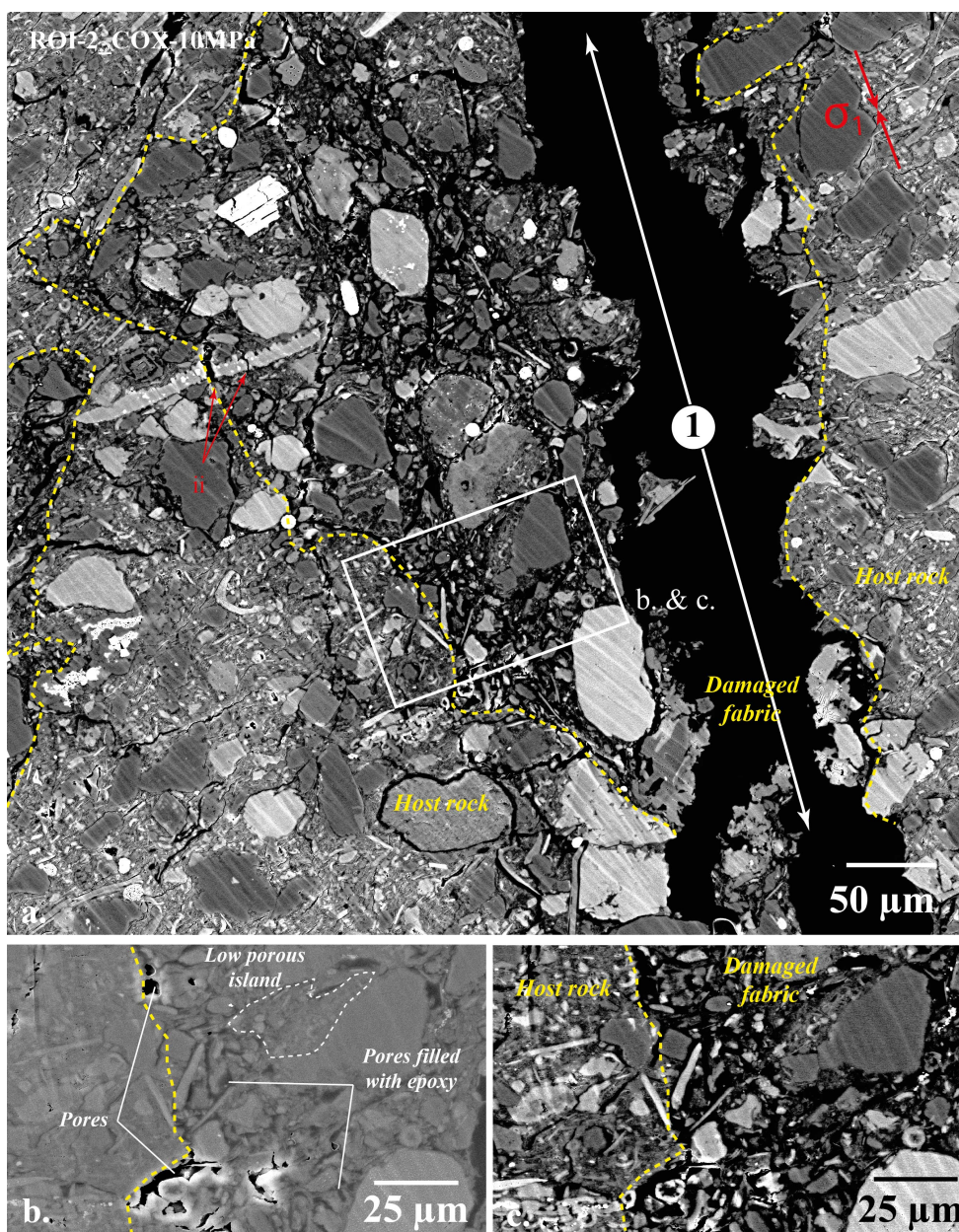
695

696

Figure 11



697



698

699

700

Figure 12